Synthesis, structure and photoelectric properties of selenide composites with in situ constructed Sb2Se3/NaSbSe2 heterojunction

D. Ren, Z. Zheng, Mx Wei, Z P. Zhang, Michel Cathelinaud, H. Ma, Xianghua Zhang

Synthesis, structure and photoelectric properties of selenide composites with in situ constructed Sb_2Se_3/$NaSbSe_2$ heterojunction

Donglou Ren[a], Zhuanghao Zheng[b], Meng Wei[a,b], Pengcheng Zhang[b], Michel Cathelinaud[a], Hongli Ma[a], Xianghua Zhang [a,*]

[a]ISCR (Institut des Sciences Chimiques de Rennes)-CNRS, UMR 6226, Univ. Rennes, F-35000, Rennes, France

[b]Shenzhen Key Laboratory of Advanced Thin Films and Applications, College of Physics and Optoelectronic engineering, Shenzhen University, Shenzhen, 518060, China

*Corresponding author: E-mail: xiang-hua.zhang@univ-rennes1.fr

Tel.: (+33) 02 23 23 69 37

Abstract

Inorganic semiconductor heterojunctions have attracted extensive attention for technological applications owing to interface phenomena. In this work, selenide composites with in situ constructed Sb_2Se_3/$NaSbSe_2$ heterojunctions with similar band gap width have been synthesized by conventional melt-quenching method. The microstructure and photoelectric properties of the composites were investigated at

different $NaSbSe_2$ contents. The study revealed that $NaSbSe_2$ content has direct influences on the photoelectric performance of the composites by modifying the heterojunction size and the grain boundary resistance, as evidenced by scanning electron microscopy and impedance spectroscopy, respectively. The photocurrent density of Sb_2Se_3 with 2.5 and 5 mol% $NaSbSe_2$ was approximately 180 times larger than that of the pure Sb_2Se_3 at a bias voltage of -1.5 V and under an illumination of 7 mW/cm^2, due to an effective separation of photogenerated carriers through the interface electric field. Additionally, the composites exhibited an excellent stability even in 0.5 M $LiClO_4$ aqueous electrolyte.

Key words: Selenide composites; Antimony selenide (Sb_2Se_3)-$NaSbSe_2$ heterojunction; Impedance spectroscopy; Photo-electro-chemical (PEC) performance; Interface electric field.

1. Introduction

In recent years, orthorhombic antimony selenide (Sb_2Se_3) is actively considered for different applications such as solar cells, photodetectors, photoelectrochemical cells, and thermoelectric devices [1-8]. This is because Sb_2Se_3 has some outstanding properties such as a narrow direct band gap (1.17 eV) [9], a high absorption coefficient ($> 10^5$ cm^{-1}) [10], a high Seebeck coefficient (1,800 μVK^{-1}) [5], and earth-abundant

constituents [11]. However, application development of the Sb_2Se_3 based materials has been limited by its intrinsically high resistivity. One possibility to overcome this challenge is to dope this material with a low-valence metal cation [12-16]. The creation of internal heterojunctions seems to be an effective way to improve different photoelectric properties. For instance, Choi et al. [5] fabricated Sb_2Se_3/Ag_2Se heterojunction nanowire that possessed a much better dark current and photocurrent, as compared to that of the intrinsic Sb_2Se_3 nanowire, to approximately 50 and 7 times, respectively. Guijarro et al. [17] constructed a Sb_2Se_3/TiO_2 heterojunction that exhibited a 3-fold improvement in the overall yield of the charge separated state upon illumination. In our previous work [18], internal Sb_2Se_3/Cu_2GeSe_3 heterojunction enhanced the photocurrent (74 $\mu A/cm^2$) that was at least 100 times higher than any of these two crystals individually (Sb_2Se_3: ~ 0.6 $\mu A/cm^2$, Cu_2GeSe_3: ~ 0.7 $\mu A/cm^2$). The enhanced photoelectric performance is attributed to the interface electric field that effectively promotes the separation and transport of photoinduced carriers.

Ternary semiconductors -the I-V-VI_2 family, where I = Cu, Ag, or alkali metals; V = Bi, Sb; and VI = S, Se, Te, have attracted increasing attention in thermoelectric [19-21] and solar cells [22-26]. Among these materials, ternary chalcogenide semiconductor $NaSbSe_2$ is another promising compound that is synthesized at high temperature with a NaCl-type structure and the lattice constant is 5.966(2) Å [27,28]. It has a narrow band gap of 1.1 eV [29] and a high absorption coefficient of 10^5 cm^{-1} at λ = 600 nm [30]. If $Sb_2Se_3/NaSbSe_2$ heterojunction can be constructed, the influence of the interface between these two materials, with different structure but similar band gap,

on the photoelectric performance will become very interesting. It is important to point out that the elements contained in the two materials are earth-abundant, low cost, nontoxic and environmentally friendly.

In the present work, the selenide composites with in situ synthesized Sb_2Se_3/$NaSbSe_2$ heterojunction have been prepared by using Sb, Se and Na elements as starting materials and by using the conventional melt-quenching method of vacuum-sealed silica tube to minimize the pollution. The influence of $NaSbSe_2$ contents on the heterojunction size and the photoelectric performance of the composites has been investigated. Ultimately, the possible mechanism of property enhancement is proposed.

2. Experimental procedure

2.1. Materials preparation

The selenide composites with internal Sb_2Se_3/$NaSbSe_2$ heterojunction were prepared by a conventional melt-quenching method. High-purity elements Sb shot (99.999%, 6 mm, Alfa Aesar), Se shot (99.999%), and Na ingot (99.95%) were used as raw materials. At first, all elements were weighted and mixed according to the appropriate stoichiometric ratio of each element (12 g mixture for each sample). The components are called SN-2.5%, SN-5%, SN-10% and SN-15%, S and N representing respectively Sb_2Se_3 and $NaSbSe_2$, and the number corresponding to the molar fraction of $NaSbSe_2$. The mixture was loaded into a carefully cleaned silica tube under protection of argon atmosphere in a glovebox. The tube has an inner diameter of 1 cm and an outer diameter 1.4 cm. Then, the tube containing all the starting elements was

pumped to a vacuum of about 10^{-5} mbar. The flame-sealed tube was placed at the center of a rocking furnace. The mixture was then heated to 700 °C with a 1.2 °C/min ramp, rocked at this temperature for 8 h to ensure a good homogenization of the melt. The tube was subsequently quenched in water to room temperature. Finally, the ingots were annealed at 350 °C for 3 h, for reducing the mechanical stress caused during the quenching process. The as-synthesized samples were then removed from the silica tube, cut and polished into 2-mm-thick discs for subsequent characterizations.

2.2. Characterization

The phases in the as-synthesized samples were determined by X-ray diffraction (XRD) using a Bruker AXS D8 Advance X-ray diffractometer (Karlsruhe, Germany) coupled with Cu-K_α radiation (λ = 1.5406 Å) in a scanning rate of 0.02° s^{-1}. The X-ray tube was operated at 40 mA and 40 kV in locked coupled mode. Scanning electron microscopy (SEM) studies were carried out on a JEOL JSM-7100F thermal field emission electron microscopy equipped with an energy dispersive X-ray spectroscopy (EDS) at 20 kV. The impedance spectroscopy and temperature-dependent conductivity were measured on an Autolab PGSTAT302N (Metrohm, AUT85901, Switzerland) in the temperature range of 278-373 K covering a frequency of 10^6-1 Hz with two stainless-steel plates as electrodes and heating sample holder. All measured samples have a diameter of 10 mm and a thickness of 2 mm. To improve the contact between the electrodes and the sample, the surface of the samples was covered with a layer of Au. Spectra analyses were performed by Zsimpwin impedance analysis software. The

photo-electro-chemical (PEC) performance of as-synthesized samples was evaluated using a three-electrode configuration, where Ag/AgCl electrode was used as the reference electrode, Pt-wire as the counter electrode and our samples as the working electrode. For obtaining the working electrode, the fine polished sample with diameter of 1 cm was connected with a copper wire by using silver paint as the back contact. Then, the sample was covered with a layer of epoxy resin for ensuring the isolation between electrode and electrolyte during the PEC measurement. The $LiClO_4$ solution (0.5 mol/L) was used as electrolyte and a white light tungsten halogen lamp was used as light source. The stability and the response speed of the photocurrent in our samples were evaluated under chopped light irradiation using a mechanical chopper. The optical property was measured with a step size of 1 nm using diffuse reflectance spectroscopy (DRS) equipped with an integrating sphere at room temperature. DRS experiments were carried out in the wavelength range of 300-2500 nm that covers the absorption zones, due to electronic transition of the semiconductor materials.

3. Results and discussion

3.1. Phase analysis and formation mechanism of composites

Fig. 1 shows the XRD patterns of as-prepared selenide composites, obtained on polished bulk samples (Fig. 1(a)) or on grinded powders (Fig. 1(b)). The standard patterns corresponding to the orthorhombic Sb_2Se_3 (JCPDS# 15-0861) and cubic

$NaSbSe_2$ (JCPDS# 77-2070) are included for reference. No other reaction products are detected in the XRD pattern of pure Sb_2Se_3. For the other samples (SN-2.5%, SN-5%, SN-10%, and SN-15%), the diffraction peaks are assigned to the orthorhombic Sb_2Se_3 and cubic $NaSbSe_2$ without other compound. For $NaSbSe_2$, the intensity of (200) and (220) peaks increases with increasing contents of $NaSbSe_2$. The XRD patterns of powders are similar to the XRD patterns of bulks, suggesting the samples prepared by melt-quenching method are homogeneous. This phenomenon was already observed in our previous works due to the mode of liquid mass transfer [31,32]. The grinding process destroyed the preferential orientation in the bulk samples, which caused some differences between the bulk and the powder in term of the relative intensity of peaks. These results suggest that the Sb_2Se_3-$NaSbSe_2$ composites were successfully prepared without impurity phase.

Because the materials were synthesized by melt-quenching method at 700 °C, the liquidus projection of the Na-Sb-Se system [27] (Fig. 2) is useful for understanding the formation mechanism. It can be seen that the largest primary crystallization field ($NaSbSe_2$) and the second-largest primary crystallization field (Na_2Se) are located in the ternary system. In addition, there is a big immiscibility area marked by dashed black line in the system. The system consists of eight binary compounds, Na_3Sb, NaSb, Sb_2Se_3, Na_2Se_x (x = 1, 2, 3, 4, 6), and the only ternary compound $NaSbSe_2$. Although there exist many binary compounds in the Na-Sb-Se system, no one is detected by XRD in Fig. 1 except Sb_2Se_3. According to previous work [33], the Na_2Se_6, Na_2Se_4, Na_2Se_3, and Na_2Se_2 decomposed at 258 °C, 290 °C, 313 °C, and 435 °C, respectively. The low

eutectic temperature of Na_3Sb and NaSb is 437 °C [34]. These binary compounds may react with each other to generate $NaSbSe_2$. Sb_2Se_3 has a negative Gibbs free energy (-38.1152 kJ mol^{-1}) at 298 K [35,36] and a low melting point of 610 °C. The local atomic arrangement in liquid is similar to that of crystalline state [37]. Consequently, we have successfully prepared Sb_2Se_3-$NaSbSe_2$ composites after quenching, as evidenced by Fig. 1.

3.2. Microstructural Characterization

The backscattered electron images and energy dispersive X-ray spectroscopy are essential for studying the distribution of phases and elements. The images of the SN-2.5% and SN-15% samples are shown in Fig. 3(a,b). It clearly illustrates that several phases are distributed in the Sb_2Se_3 matrix with different sizes. To further determine the composition of these phases, the EDS was used to measure the composition of the points 1, 2 and 3 in Fig. 3(b), as shown as Table 1. It suggests that the point 1 is Se, point 2 is $NaSbSe_2$ and point 3 is Sb_2Se_3. It is observed that the Se is distributed around $NaSbSe_2$. The residual Se may be due to the imbalance of local compositions in liquid during melting or quenching process. According to a previous report [35], the liquidus Se and Sb_2Se_3 have a strong tendency toward immiscibility in some range of Se atomic percent. Moreover, there is a big immiscibility area [27] in Na-Sb-Se system (Fig. 2). The existence of Se in the composites has not been detected in XRD patterns (Fig. 1) due to the low content. The EDS elemental mappings of the SN-15% sample further proves that the distribution of elements is globally homogenous except few selenium

rich domains (Fig. 3(c-e)). The distribution of Na element is quite uniform (Fig. 3(e)), because of the globally low content level, leading to high noisy background.

In order to observe the grain size of composites, the surface of the SN-15% sample was etched with a solution of 1 mol/L NaOH at ambient temperature. As shown in Fig. 4, it can be seen that the sample consists of Sb_2Se_3 (Na-doped, white) and $NaSbSe_2$ grains (gray) from the composition shown in Table 2 except the black holes. The average grain sizes of Sb_2Se_3 and $NaSbSe_2$ are approximately 50 μm and 5 μm, respectively. The EDS elemental mapping further reveals that the $NaSbSe_2$ has a homogeneous distribution in Sb_2Se_3. The formation mechanism of such microstructure can be explained as follows: in the liquidus, $NaSbSe_2$ and Sb_2Se_3 are phase separated due to their immiscibility observed in Fig. 2. A small amount of $NaSbSe_2$ phase precipitates firstly due to its higher melting point (740 °C) [27] and the crystals are randomly distributed in liquid Sb_2Se_3 which will crystallize afterwards. The same phenomenon was observed in SN-5% and SN-10% samples (not shown). These results indicate that the Sb_2Se_3/$NaSbSe_2$ heterojunctions were successfully in situ constructed by conventional melt-quenching method. It is generally observed that interface quality is often excellent when it is obtained by crystallization of liquid phases.

To further confirm the existence of heterojunctions inside the composites, the I-V curve of the SN-2.5% sample was characterized by using sputtered two gold contacts on the top and bottom surfaces (Fig. 5). The I-V curve displays a non-ohmic character, indicating that the SN-2.5% specimen contains internal heterojunctions, which is randomly distributed as shown in Fig. 3(a).

3.3. UV-vis diffuse reflectance spectroscopy

The band gap of a semiconductor material is an important characteristic, which can be obtained by measuring the optical diffuse reflectance of the powders. The absorption spectra of all samples was converted from diffuse reflectance data by using the Kubelka-Munk and Tauc functions (Supporting Information). The band gap energy is then calculated by linear fit of the $(F(R)\cdot h\nu)^2 = B(h\nu - E_g)$ and the results are shown in Fig. 6 and Table 3 for all the samples. The band gap energy of pure $NaSbSe_2$ (1.21 eV) is higher than literature data (1.1 eV) [29], which is related to intrinsic defects obtained by different synthesis methods and conditions [38]. It can also be seen that the direct band gap of pure Sb_2Se_3 sample is 1.15 eV in agreement with previous work [10]. For the composites with internal $Sb_2Se_3/NaSbSe_2$ heterojunction, the direct band gaps are close to 1.17 eV. The narrow band gap energy would lead to a strong absorption of the solar spectrum.

3.4. Impedance spectroscopy

The electrical conductivity of different samples with a thickness of 2 mm and a diameter of 10 mm was measured by using impedance spectroscopy. Fig. 7 shows the variation of impedance real (Z′) part, impedance imaginary (Z″) part, and normalized Z″ with frequency at different temperatures for two representative samples SN-2.5% and SN-15%. It can be seen that the real part (Z′) of impedance decreases with increasing temperatures, corresponding to the behaviors of semiconductors [39].

According to previous works [40,41], Sb_2Se_3 and $NaSbSe_2$ have a large number of intrinsic defects, such as V_{Se}, V_{Na}, Na_{Sb}, Sb_{Se}. The space charge effect is a dominant process at low temperatures and high frequencies, and in contrast, the space charge polarization is positive at low frequencies and high temperatures in term of Z' [42]. The Z' drastically reduces with increasing frequency, suggesting the space charge polarization [43] exists in these samples. The variation of imaginary part of impedance (Z'') with frequency at different temperatures, can be used to evaluate the relaxation frequency. It can be seen that the Z'' has a maximum peak with frequency at different temperatures (Fig. 7(b,e)). This peak in Z'' shifts towards high frequencies with increasing temperature and $NaSbSe_2$ content, which illustrates a decrease in the relaxation time and a thermally activated relaxation in the system [44]. A lower relaxation time implies faster movement of mobile charge carriers in the samples due to the existence of Sb_2Se_3/$NaSbSe_2$ heterojunction. The peak broadening at high temperatures, suggests that the temperature dependent relaxation process exists in theses materials [43]. The asymmetric broadening of peaks also illustrates the presence of electrical processes in the material with a spread of relaxation time as indicated by changes in peak width [45]. The relaxation may be caused by immobile species at low temperature and defects (vacancies, interstitials, and antisites) at higher temperature. The electrical conduction in the material is realized by hopping of electrons among the available localized sites [40,41,46,47]. The phenomenon was also observed in the normalized Z'' with frequency in Fig. 7(c, f). Moreover, the magnitude of Z'' declines with shifting peak frequency to high frequency direction with increase of $NaSbSe_2$

content. This may be due to the accumulation of space charge in all materials in the high frequency zone. Similar result was also reported by other authors [46].

The Nyquist plots and the variation of conductivity with temperature were shown in Fig. 8. The asymmetric semicircular arcs appear in the impedance plot (Fig. 8(a,b)). The symmetry of semicircular arc depends on the nature of the material or its history [48]. The spectrum consists of single semicircular arc, which shrinks with increasing temperature. It further suggests that the all samples are semiconductors with a negative temperature coefficient of resistance. The bulk and grain boundaries effects exist in polycrystalline materials [49]. For selenide composites (SN-2.5% and SN-15%) with internal Sb_2Se_3/$NaSbSe_2$ heterojunctions, the plots include two semicircular arcs whose center is located below the real axis. The plots display the phenomena of semi-circle decentralization in the composites, which is frequently observed [50]. It can be seen that the electrical response is consisted of two overlapped semicircles. Due to the similar relaxation frequency, the high overlapping degree exists in the two semicircles. The first relaxation reflects the grains or bulk at high frequency and the second relaxation corresponds to the grain boundaries at low frequency. In our impedance spectra, the lack of electrode effect (line tail) in the range of experimental temperature indicates that all samples are electronic conductors, rather than ionic conductors.

According to the Debye's model, a material should be an ideal semicircle with the center on the real axis because of a single relaxation time [51]. However, the relaxation process is non-Debye type in our materials [52], due to the grain size, grain boundaries, grain orientation, defect distribution, etc [53]. In order to better understand the electrical

response in materials, an equivalent circuit is necessary for fitting the measured data. The electrical properties are well illustrated by two parallel elements (R_bC_b-$R_{gb}C_{gb}$) and R_0 in series for these composites at 25 °C in Fig. 8(c), where C_b = bulk capacitance; C_{gb} = grain boundaries capacitance; R_b = bulk resistance; and R_{gb} = grain boundary resistance. The equivalent circuits of pure Sb_2Se_3 and $NaSbSe_2$ can be found in Fig. S4 (Supporting Information). R_0 corresponds to the high frequency intersection ($R_0 = 0$ for pure compounds), which is related to pores, capillary cavities, micro-cracks and even external contacts resistance [54-56]. It can be observed that these materials have a strong temperature dependence of conductivity (Fig. 8(d)). The curve was fitted by Arrhenius relation and activation energy for electrical conduction was obtained from the slope of the fitted lines. The equivalent circuit best fitted to measured data and the values of R_0, R_b, and R_{gb}, resistivity at 25 °C, and activation energy are shown in Table 4. The $NaSbSe_2$ has a bulk resistance of 8.63×10^3 Ω and a much higher grain boundary resistance of 1.44×10^6 Ω. However, the grain boundary resistance (2.60×10^5 Ω) is close to the bulk resistance (4.02×10^5 Ω) for Sb_2Se_3. This may relate to the crystalline structure of Sb_2Se_3 composed of intrinsic one dimensional $(Sb_4Se_6)_n$ ribbons with no dangling bonds at the edge, corresponding to grain boundaries [57]. However, $NaSbSe_2$ has a NaCl-type three-dimensional structure [58] that has an isotropic carrier transport and dangling bonds at grain boundaries. The dangling bonds typically act as recombination centers in three-dimensional crystal structure, such as Si, GaAs, CdTe, InP, and Cu(In,Ga)Se_2 (CIGS), which can be minimized by using different techniques including chemical surface/defect passivation and appropriate thermal processing [59-

61]. Further, the concentration, the type and the distribution of defects in grain boundary and bulk/grain may be another reason for the difference in bulk and grain boundary resistance. The resistivity of Sb_2Se_3 and $NaSbSe_2$ is 2.14×10^6 Ω·cm and 8.87×10^5 Ω·cm, respectively. For the composites with internal Sb_2Se_3/$NaSbSe_2$ heterojunctions, the resistivity is reduced with increasing $NaSbSe_2$ contents, which is related to the interface defects. Similar work was also reported by O. Dier et al [62].

The activation energy, reflecting the energy for the hopping of electrons, of all Sb_2Se_3/$NaSbSe_2$ composites is between the quite similar values for pure Sb_2Se_3 and $NaSbSe_2$ (between 0.45 - 0.61 eV). It means that the activation energy is mainly governed by the hoping of electrons inside Sb_2Se_3 or $NaSbSe_2$. Therefore, the grain boundaries and the Sb_2Se_3/$NaSbSe_2$ interfaces are not difficult barriers for electrons to cross.

3.5. Photo-electro-chemical (PEC) performance

In order to explore the influence of heterojunction interface on the PEC performance of composites, the three-electrode configuration (Inset in Fig. 9) was used at ambient temperature. As shown in Fig. 9, all samples show cathodic photocurrents and their photocurrent density increases with increasing cathodic potential, indicating these materials are p-type semiconductors. The difference between dark and light current represents the photocurrent density. The photocurrent densities of pure Sb_2Se_3 and $NaSbSe_2$ are very weak (less than 1 μA/cm^2) (Fig. S5, Supporting Information), due to the absence of internal heterojunction that could effectively separate

photogenerated carriers based on the interface electric field. Similar results can also be obtained in our previous works [16,18]. However, very important increase of photocurrent density has been observed in composites with internal heterojunctions. The values of photocurrent density (SN-2.5%: -139.87 μA/cm^2, SN-5%: -134.37 μA/cm^2, SN-10%: -44.26 μA/cm^2, and SN-15%: -72.47 μA/cm^2) at a bias voltage of -1.5 V are first reduced and then increased with increasing $NaSbSe_2$ contents. It can be explained as follows: Firstly, the internal heterojunctions could promote the separation of photogenerated electron-hole pairs, thanks to the interface electric field, and therefore prolong the carrier lifetime, resulting in higher photocurrent density when $NaSbSe_2$ content was low. The photocurrent densities of SN-2.5% and SN-5% samples are 139.87 μA/cm^2 and 134.37 μA/cm^2, respectively, which are approximately 180 times larger than that of pure Sb_2Se_3 (less than 1 μA/cm^2). Secondly, the number of $NaSbSe_2$/$NaSbSe_2$ grain boundaries increased with increasing $NaSbSe_2$ contents, resulting in fewer Sb_2Se_3/$NaSbSe_2$ interface. Meanwhile, the $NaSbSe_2$/$NaSbSe_2$ grain boundaries could cause higher recombination due to the three-dimensional structure and the dangling bonds at grain boundaries. This is illustrated by the recombination resistance [63] (grain boundary resistance) in Table 4. A larger recombination resistance suggests a lower rate of recombination [64]. The grain boundary resistance decreased with increasing $NaSbSe_2$ content for SN-10% sample, which caused the decreases of photocurrent density due to increased recombination of photogenerated carriers. Finally, the grain size of $NaSbSe_2$ is increased in SN-15% sample with increasing $NaSbSe_2$ content (Fig. 3), accompanied by increased area of Sb_2Se_3/$NaSbSe_2$ heterojunction

interface. Compared with the reduced number of Sb_2Se_3/$NaSbSe_2$ interfaces, the increased area will become the dominant factor affecting the photocurrent density. Consequently, the photocurrent density of this sample is higher than that of SN-10% due to the effective separation of photogenerated carriers [65,66]. These results illustrate that the photoelectric properties of selenide composites are significantly enhanced through interface electric field of Sb_2Se_3/$NaSbSe_2$ heterojunction.

Furthermore, the cyclic photoresponse of the pure Sb_2Se_3 and selenide composites was characterized (Fig. 10(a)). When the light is turned on, the current densities quickly increase from -1.27 μA/cm^2 (dark) to -1.35 μA/cm^2 (light) for Sb_2Se_3 at a bias of -0.7 V. In contrast to Sb_2Se_3, the SN-5% sample has a much higher current density that increases from -4.56 μA/cm^2 (dark) to -10.93 μA/cm^2 (light) due to the interface electric field of heterojunction. Additionally, the current density drops once light is switched off. Sb_2Se_3 shows a sharp decrease with a recovery time (τ_{off}) of 0.029 s, whereas all composites both show a slower decay such as SN-5% sample with τ_{off} of 0.076 s (Fig. S8, Supporting Information). This slow decay could be associated with the presence of charge trap centers and other defect states in composites, as already found in previous reports [67-69]. The photoresponse has not significant difference during at least 10 cycles, revealing the excellent stability of the selenide composites with internal heterojunctions. The speed of rise and fall for photocurrent is a good indicator of the photosensitivity for a material. Moreover, the photosensitivity (S_{ph}) of Sb_2Se_3 and composites was calculated by the following formula: $S_{ph} = (I_L - I_D)/I_D = (J_{ph} - J_d)/J_d$ [67], where I_L, I_D, J_{ph}, and J_d represent illuminated current, dark current, photocurrent density,

and dark current density, respectively. The S_{ph} values are 0.049, 1.638, 2.102, 2.000, and 1.870 for pure Sb_2Se_3, SN-2.5%, SN-5%, SN-10%, and SN-15% samples, respectively. It is obvious that the S_{ph} value of pure Sb_2Se_3 is much lower than that of the composites. It further proved that the composites with internal heterojunctions have much better photosensitivity, resulting in the higher photocurrent density (approximately 180 times) as compared to Sb_2Se_3.

Fig. 10(b) displays the relationship between the incident light intensity and the current density at a bias voltage of -0.7 V. The relation can be expressed as $J_{ph} \propto P^{\theta}$, where J_{ph} is the photocurrent density, P is the power density of the incident light, and θ is an exponent [16]. The θ value was obtained by linear fitting in the form of double log-plot. All θ values are smaller than that of low trap state (θ = 1), which can be attributed to the complex process of carriers generation, trapping and recombination in composites [70].

3.6. Mechanism of the enhanced PEC performance

On the basis of the above results, the possible mechanism of the enhanced PEC performance of composites is proposed (Fig. 11). The valence band (VB) and the conduction band (CB) potential of Sb_2Se_3 and $NaSbSe_2$ can be calculated by the following empirical formulae [71,72]: $E_{VB} = X - E^e + 0.5\ E_g$ and $E_{CB} = E_{VB} - E_g$, where E_{VB} is the VB edge potential, E_{CB} is the CB edge potential, E_g is the band gap energy of the semiconductor, X is the electronegativity of the semiconductor, and the values of Sb_2Se_3 and $NaSbSe_2$ were calculated according to the electronegativity of the constitute

atoms [73]. E^e is the energy of free electrons on the hydrogen scale (~ 4.5 eV). As a result, the X values for Sb_2Se_3 and $NaSbSe_2$ are 5.41 eV and 4.66 eV, respectively. The VB and CB of Sb_2Se_3 were separately calculated to be 1.48 eV and 0.34 eV. Similarly, the VB and CB of $NaSbSe_2$ correspond to 0.76 eV and -0.44 eV, respectively. The Fermi level of $NaSbSe_2$ is pinned at 0.45 eV above VB from the early report [40]. The Fermi level in Sb_2Se_3 laid in the middle of CB and VB [74] that located at 0.91 eV, which helps us to draw the band diagram. When Sb_2Se_3 and $NaSbSe_2$ contact with each other, the heterojunction interface is formed with an electric field. Both of Sb_2Se_3 and $NaSbSe_2$ can be easily excited and produce electron-hole pairs under visible light illumination due to their narrow direct band gaps. The photoinduced electrons could more easily transfer from the CB bottom of $NaSbSe_2$ to that of Sb_2Se_3 under the effect of interface electric field, while the holes left on the VB top of Sb_2Se_3 moved in the opposite direction to VB top of $NaSbSe_2$. Therefore, the heterojunction interface, not only improves the separation efficiency of the photogenerated electrons and holes, but also prolong the lifetime of photoinduced carriers, leading to higher photocurrent density.

4. Conclusion

Selenide composites with in situ synthesized Sb_2Se_3/$NaSbSe_2$ heterojunctions based on two materials having close band gap energy were successfully prepared via the reaction among Sb, Se and Na by using conventional melt-quenching method, which is favourable for forming a high-quality solid-solid interface without pollution.

The impedance spectroscopy shows that the composites are electronic conductors and the photo-electro-chemical measurement reveals that the composites have a p-type conducting characteristics. The photocurrent density of composites is firstly reduced and then increased with increasing $NaSbSe_2$ contents, which is related to the decreased grain boundary resistance and increased heterojunction size. The interface electric field of the $Sb_2Se_3/NaSbSe_2$ heterojunctions helped effectively the separation of the photogenerated electron-hole pairs. The photocurrent density of Sb_2Se_3 with 2.5 and 5 mol% $NaSbSe_2$ contents was approximately 180 times larger than that of the pure Sb_2Se_3 at a bias voltage of -1.5 V and under an illumination of 7 mW/cm^2. Additionally, the composites exhibited an excellent stability even in 0.5 M $LiClO_4$ aqueous electrolyte. Considering the enhanced photocurrent density and the excellent stability, the selenide composite with internal $Sb_2Se_3/NaSbSe_2$ heterojunctions can be considered as a promising candidate for PEC water splitting and photocatalysis.

Declaration of interests

The authors declare that they have no known competing financial interests or personal relationships that could have appeared to influence the work reported in this paper.

Acknowledgements

This research was supported by CNRS and Université de Rennes 1. We gratefully acknowledge the Chinese Scholarship Council of PR China for providing financial support (201804910786) for D.R. to stay at the ISCR.

References

[1] S. Messina, M.T.S. Nair, P.K. Nair, Antimony Selenide Absorber Thin Films in All-Chemically Deposited Solar Cells, J. Electrochem. Soc. 156 (2009) H327-H332.

[2] Z. Li, X. Liang, G. Li, H. Liu, H. Zhang, J. Guo, J. Chen, K. Shen, X. San, W. Yu, R.E. Schropp, Y. Mai, 9.2%-efficient core-shell structured antimony selenide nanorod array solar cells, Nat. Commun. 10 (2019) 125-133.

[3] J. Zhang, R. Kondrotas, S. Lu, C. Wang, C. Chen, J. Tang, Alternative back contacts for Sb_2Se_3 solar cells, Sol. Energy 182 (2019) 96-101.

[4] L. Wang, D.B. Li, K. Li, C. Chen, H.X. Deng, L. Gao, Y. Zhao, F. Jiang, L. Li, F. Huang, Y. He, H. Song, G. Niu, J. Tang, Stable 6%-efficient Sb_2Se_3 solar cells with a ZnO buffer layer, Nat. Energy 2 (2017) 17046.

[5] D. Choi, Y. Jang, J. Lee, G.H. Jeong, D. Whang, S.W. Hwang, K.S. Cho, S.W. Kim, Diameter-Controlled and Surface-Modified Sb_2Se_3 Nanowires and Their Photodetector Performance, Sci. Rep. 4 (2015) 6714.

[6] R.R. Prabhakar, W. Septina, S. Siol, T. Moehl, R. Wick-Joliat, S.D. Tilley, Photocorrosion-resistant Sb_2Se_3 photocathodes with earth abundant MoS_x hydrogen evolution catalyst, J. Mater. Chem. A 5 (2017) 23139-23145.

[7] J. Park, W. Yang, Y. Oh, J. Tan, H. Lee, R. Boppella, J. Moon, Efficient Solar-to-Hydrogen Conversion from Neutral Electrolytes using Morphology-Controlled Sb_2Se_3 Light Absorbers, ACS Energy Lett. 4 (2019) 517-526.

[8] D. An, S. Chen, Z. Lu, R. Li, W. Chen, W. Fan, W. Wang, Y. Wu, Low Thermal Conductivity and Optimized Thermoelectric Properties of p-Type Te-Sb_2Se_3: Synergistic Effect of Doping and Defect Engineering, ACS Appl. Mater. Interfaces 11 (2019) 27788-27797.

[9] C. Chen, Y. Yang, D.C. Bobela, S. Lu, K. Zeng, B. Yang, L. Gao, M.C. Beard, J. Tang, Characterization of basic physical properties of Sb_2Se_3 and its relevance for photovoltaics, Front. Optoelectron. 10 (2017) 18-30.

[10] C. Chen, W. Li, Y. Zhou, C. Chen, M. Luo, X. Liu, K. Zeng, B. Yang, C. Zhang, J. Han, J. Tang, Optical properties of amorphous and polycrystalline Sb_2Se_3 thin films prepared by thermal evaporation, Appl. Phys. Lett. 107 (2015) 043905.

[11] X. Wen, Y. He, C. Chen, X. Liu, L. Wang, B. Yang, M. Leng, H. Song, K. Zeng, D. Li, K. Li, L. Gao, J. Tang, Magnetron sputtered ZnO buffer layer for Sb_2Se_3 thin film solar cells, Sol. Energy Mater. Sol. Cells 172 (2017) 74-81.

[12] W. Wu, Y. Li, L. Liang, Q. Hao, J. Zhang, H. Liu, C. Liu, Enhanced Broadband Responsivity of Ni-Doped Sb_2Se_3 Nanorod Photodetector, Phys. Chem. C 123 (2019) 14781-14789.

[13] Y. Zhou, Y. Li, J. Luo, D. Li, X. Liu, X. Liu, C. Chen, H. Song, J. Ma, D.J. Xue, B. Yang, J. Tang, Buried homojunction in CdS/Sb_2Se_3 thin film photovoltaics generated by interfacial diffusion, Appl. Phys. Lett. 111 (2017) 013901.

[14] Y. Li, Y. Zhou, Y. Zhu, C. Chen, J. Luo, J. Ma, B. Yang, X. Wang, Z. Xia, J. Tang, Characterization of Mg and Fe doped Sb_2Se_3 thin films for photovoltaic application, Appl. Phys.

Lett. 109 (2016) 232104.

[15] J. Choi, H.W. Lee, B.S. Kim, H. Park, S. Choi, S.C. Hong, S. Cho, Magnetic and transport properties of Mn-doped Bi_2Se_3 and Sb_2Se_3, 304 (2006) 164-166.

[16] S. Chen, X. Qiao, Z. Zheng, M. Cathelinaud, H. Ma, X. Fan, X. Zhang, Enhanced electrical conductivity and photoconductive properties of Sn-doped Sb_2Se_3 crystals, J. Mater. Chem. C. 6 (2018) 6465-6470.

[17] N. Guijarro, T. Lutz, T. Lana-Villarreal, F. O'Mahony, R. Gómez, S.A. Haque, Toward Antimony Selenide Sensitized Solar Cells: Efficient Charge Photogeneration at spiro-OMeTAD/Sb_2Se_3/Metal Oxide Heterojunctions, J. Phys. Chem. Lett. 3 (2012) 1351-1356.

[18] X. Zhang, Y. Xu, Q. Shen, B. Fan, X. Qiao, X. Fan, H. Yang, Q. Luo, L. Calvez, H. Ma, M. Cathelinaud, J.J. Simon, Enhancement of charge photo-generation and transport via an internal network of Sb_2Se_3/Cu_2GeSe_3 heterojunctions, J. Mater. Chem. A 2 (2014) 17099-17106.

[19] S.N. Guin, V. Srihari, K. Biswas, Promising thermoelectric performance in n-type $AgBiSe_2$: effect of aliovalent anion doping, J. Mater. Chem. A 3 (2015) 648-655.

[20] C. Xiao, X. Qin, J. Zhang, R. An, J. Xu, K. Li, B. Cao, J. Yang, B. Ye, Y. Xie, High Thermoelectric and Reversible p-n-p Conduction Type Switching Integrated in Dimetal Chalcogenide, J. Am. Chem. Soc. 134 (2012) 18460-18466.

[21] S.N. Guin, A. Chatterjee, D.S. Negi, R. Datta, K. Biswas, High thermoelectric performance in tellurium free p-type $AgSbSe_2$, Energy Environ. Sci. 6 (2013) 2603-2608.

[22] C.L. Chou, N. Suriyawong, B. Aragaw, J.B. Shi, M.W. Lee, Ag_3SbS_3 Liquid-Junction Semiconductor-Sensitized Solar Cells, J. Electrochem. Soc. 163 (2016) H445-H449.

[23] N. Liang, W. Chen, F. Dai, X. Wu, W. Zhang, Z. Li, J. Shen, S. Huang, Q. He, J. Zai, N. Fang, X. Qian, Homogenously hexagonal prismatic $AgBiS_2$ nanocrystals: controlled synthesis and application in quantum dot-sensitized solar cells, CrystEngComm 17 (2015) 1902-1905.

[24] Z. Liu, J. Huang, J. Han, T. Hong, J. Zhang, Z. Liu, $CuSbS_2$: a promising semiconductor photo-absorber material for quantum dot sensitized solar cells, Phys. Chem. Chem. Phys. 18 (2016) 16615–16620.

[25] M. Bernechea, N. C. Miller, G. Xercavins, D. So, A. Stavrinadis, G. Konstantatos, Solution-processed solar cells based on environmentally friendly $AgBiS_2$ nanocrystals, Nat. Photonics 10 (2016) 521–525.

[26] N. Suriyawong, B. Aragaw, J.B. Shi, M.W. Lee, Ternary $CuBiS_2$ nanoparticles as a sensitizer for quantum dot solar cells, J. Colloid Interface Sci. 473 (2016) 60–65.

[27] A.V. Salov, V.B. Lazarev, I.S. Shaplygin, Phase diagram of the system A(I)-B(V)-C(VI). II. Ternary system Na-Sb-Se, Thermochim. Acta 32 (1979) 57-62.

[28] K. Hoang, S.D. Mahanti, Atomic and electronic structures of I-V-VI_2 ternary chalcogenides, J. Sci.: Adv. Mater. Dev. 1 (2016) 51-56.

[29] T.J. Slade, T.P. Bailey, J.A. Grovogui, X. Hua, X. Zhang, J.J. Kuo, I. Hadar, G.J. Snyder, C. Wolverton, V.P. Dravid, C. Uher, M.G. Kanatzidis, High Thermoelectric Performance in PbSe–$NaSbSe_2$ Alloys from Valence Band Convergence and Low Thermal Conductivity, Adv. Energy Mater. 9 (2019) 1901377.

[30] V.A. Bazakutsa, N.I. Gnidash, A.K. Kul'chitskaya, A.V. Salov, Photoelectric and optical properties of thin films of ternary chalcogenides of the form $Me^{I}SbX_{VI}^{2}$, Phys. Usp. 18 (1975) 472-475.

[31] D. Ren, Q. Deng, J. Wang, Y. Li, M. Li, S. Ran, S. Du, Q. Huang, Densification and mechanical

properties of pulsed electric current sintered B_4C with in situ synthesized Al_3BC obtained by the molten-salt method, J. Eur. Ceram. Soc. 37 (2017) 4524-4531.

[32] D. Ren, Q. Deng, J. Wang, J. Yang, Y. Li, J. Shao, M. Li, J. Zhou, S. Ran, S. Du, Q. Huang, Synthesis and properties of conductive B_4C ceramic composites with TiB_2 grain network, J. Am. Ceram. Soc. 101 (2018) 3780-3786.

[33] J. Sangster, A.D. Pelton, The Na-Se (Sodium-Selenium) System, J. Phase Equilib. 18 (1997) 185-189.

[34] Y. Liu, J. Xu, Z. Kang, J. Wang, Thermodynamic descriptions and phase diagrams for Sb–Na and Sb–K binary systems, Thermochim. Acta 569 (2013) 119-126.

[35] G. Ghosh, The sb-se (antimony-selenium) system, J. Phase Equilib. 14 (1993) 753-763.

[36] Y. Zhou, M. Leng, Z. Xia, J. Zhong, H. Song, X. Liu, B. Yang, J. Zhang, J. Chen, K. Zhou, J. Han, Y. Cheng, J. Tang, Solution-Processed Antimony Selenide Heterojunction Solar Cells, Adv. Energy Mater. 4 (2014) 1301846.

[37] T. Satow, O. Uemura, S. Akaike, S. Tamaki, The structure analysis liquid Sb_2Se_3 by neutron diffraction, J. Non-Cryst. Solids 29 (1978) 215-221.

[38] R.A.C. Amoresi, V. Teodoro, G.F. Teixeira, M.S. Li, A.Z. Simões, L.A. Perazolli, E. Longo, M.A. Zaghete, Electrosteric colloidal stabilization for obtaining $SrTiO_3/TiO_2$ heterojunction: Microstructural evolution in the interface and photonics properties, J. Eur. Ceram. Soc. 38 (2018) 1621-1631.

[39] C.F. Yang, Improvement of the Sintering and Dielectric Characteristics of Surface Barrier Layer Capacitors by CuO Addition, Jpn. J. Appl. Phys. 35 (1996) 1806-1813.

[40] C.M. Dai, P. Xu, M. Huang, Z.H. Cai, D. Han, Y. Wu, S. Chen, $NaSbSe_2$ as a promising light-absorber semiconductor in solar cells: First-principles insights, APL Mater. 7 (2019) 081122.

[41] X. Liu, X. Xiao, Y. Yang, D.J. Xue, D.B. Li, C. Chen, S. Lu, L. Gao, Y. He, M.C. Beard, G. Wang, S. Chen, J. Tang, Enhanced Sb_2Se_3 solar cell performance through theory-guided defect control, Prog. Photovolt: Res. Appl. 25 (2017) 861-870.

[42] A. Kaushal, S.M. Olhero, B. Singh, D.P. Fagg, I. Bdikin, J.M.F. Ferreira, Impedance analysis of $0.5Ba(Zr_{0.2}Ti_{0.8})O_3–0.5(Ba_{0.7}Ca_{0.3})TiO_3$ ceramics consolidated from micro-granules, Ceram. Int. 40 (2014) 10593-10600.

[43] A.K. Jonscher, The 'universal' dielectric response, Nature 267 (1977) 673-679.

[44] D.C. Sinclair, A.R. West, Impedance and modulus spectroscopy of semiconducting $BaTiO_3$ showing positive temperature coefficient of resistance, J. Appl. Phys. 66 (1989) 3850-3856.

[45] S. Brahma, R.N.P. Choudhary, A.K. Thakur, AC impedance analysis of $LaLiMo_2O_8$ electroceramics, Phys. B: Phys. Cond. Matter 355 (2005) 188-201.

[46] A. Kumar, R.N.P. Choudhary, B.P. Singh, A.K. Thakur, Effect of strontium concentration on electrical conduction properties of Sr-modified $BaSnO_3$, Ceram. Int. 32 (2006) 73-83.

[47] B.R. Chakraborty, B. Ray, R. Bhattachary, A.K. Dutta, Magnetic and electric properties of antimony selenide (Sb_2Se_3) crystals, J. Phys. Chem. Solids 41 (1980) 913-917.

[48] M. Sahu, R.N.P. Choudhary, S.K. Das, S. Otta, B.K. Roul, Inter-grain mediated intrinsic and extrinsic barrier layer network mechanism involved in $Ca_1Cu_3Ti_4O_{12}$ bulk ceramic, J. Mater. Sci.: Mater. Electron. 28 (2017) 15676-15684.

[49] J. R. Macdonald, Impedance Spectroscopy: Emphasizing Solid-State Material and Systems, Wiley, 1987.

[50] K. Verma, S. Sharma, Impedance spectroscopy and dielectric behavior in barium strontium

titanate-nickel zinc ferrite composites, Phys. Status Solidi B 249 (2012) 209-2016.

[51] M.N. Rahaman, Ceramic Processing and Sintering, Marcel Dekker, 1995.

[52] B.K. Barick, K.K. Mishra, A.K. Arora, R.N.P. Choudhary, D.K. Pradhan, Impedance and Raman spectroscopic studies of $(Na_{0.5}Bi_{0.5})TiO_3$, J. Phys. D Appl. Phys. 44 (2011) 355402.

[53] S. Sen, R.N.P. Choudhary, A. Tarafdar, P. Pramanik, Impedance spectroscopy study of strontium modified lead zirconate titanate ceramics, J. Appl. Phys 99 (2006) 124114.

[54] G. Song, Equivalent circuit model for AC electrochemical impedance spectroscopy of concrete, Cem. Concr. Res. 30 (2000) 1723-1730.

[55] K. Srinivas, P. Sarah, S.V. Suryanarayana, Impedance spectroscopy study of polycrystalline $Bi_6Fe_2Ti_3O_{18}$, Bull. Mater. Sci. 26 (2003) 247-253.

[56] J. Ângelo, P. Magalhães, L. Andrade, A. Mendes, Characterization of TiO_2-based semiconductors for photocatalysis by electrochemical impedance spectroscopy, Appl. Surf. Sci. 387 (2016) 183-189.

[57] Y. Zhou, L. Wang, S. Chen, S. Qin, X. Liu, J. Chen, D. J. Xue, M. Luo, Y. Cao, Y. Cheng, E. H. Sargent, J. Tang, Thin-film Sb_2Se_3 photovoltaics with oriented one-dimensional ribbons and benign grain boundaries, Nat. Photonics 9 (2015) 409-415.

[58] S.N. Guin, K. Biswas, Temperature driven p–n–p type conduction switching materials: current trends and future directions, Phys. Chem. Chem. Phys. 17 (2015) 10316-10325.

[59] R. Baier, C. Leendertz, D. Abou-Ras, M.C. Lux-Steiner, S. Sadewasser, Properties of electronic potential barriers at grain boundaries in $Cu(In,Ga)Se_2$ thin films, Sol. Energ. Mat. Sol. C 130 (2014) 124-131.

[60] Y.C. Choi, D.U. Lee, J.H. Noh, E.K. Kim, S.I. Seok, Highly Improved Sb_2S_3 Sensitized-Inorganic-Organic Heterojunction Solar Cells and Quantification of Traps by Deep-Level Transient Spectroscopy, Adv. Funct. Mater. 24 (2014) 3587-3592.

[61] S.B. Zhang, S-H. Wei, A. Zunger, H. Katayama-Yoshida, Defect physics of the $CuInSe_2$ chalcopyrite semiconductor, Phys. Rev. B 57 (1998) 9642-9656.

[62] O. Dier, C. Reindl, A. Bachmann, C. Lauer, T. Lim, K. Kashani-Shirazi, M.C. Amann, Reduction of hetero-interface resistivity in n-type AlAsSb/GaSb distributed Bragg reflectors, Semicond. Sci. Technol. 23 (2008) 025018-025021.

[63] H. Kim, H. Jeong, T.K. An, C.E. Park, K. Yong, Hybrid-Type Quantum-Dot Cosensitized ZnO Nanowire Solar Cell with Enhanced Visible-Light Harvesting, ACS Appl. Mater. Interfaces 5 (2013) 268-275.

[64] M. Basu, N. Garg, A.K. Ganguli, A type-II semiconductor (ZnO/CuS heterostructure) for visible light photocatalysis, J. Mater. Chem. A 2 (2014) 7517-7525.

[65] M. Tayebi, A. Tayyebi, B.-K. Lee, C.-H. Lee, D.-H. Lim, The effect of silver doping on photoelectrochemical (PEC) properties of bismuth vanadate for hydrogen production, Sol. Energy Mater. Sol. Cells 200 (2019) 109943.

[66] C.H. Chen, J. Shieh, H.Y. Liao, J.J. Shyue, Construction of titania–ceria nanostructured composites with tailored heterojunction for photocurrent enhancement, J. Eur. Ceram. Soc. 34 (2014) 1523-1535.

[67] C.J. Diliegros-Godines, J.S. Cruz, N.R. Mathews, M. Pal, Effect of Ag doping on structural, optical and electrical properties of antimony sulfide thin films, J. Mater. Sci. 53 (2018) 11562-11573.

[68] Y.Q. Liu, M. Zhang, F.X. Wang, G.B. Pan, Facile microwave-assisted synthesis of uniform Sb_2Se_3 nanowires for high performance photodetectors, J. Mater. Chem. C 2 (2014) 240-244.

[69] K.A. Sablon, A. Sergeev, S. Najmaei, M. Dubey, High-response hybrid quantum dots-2D conductor phototransistors: recent progress and perspectives, Nanophotonics 6 (2017) 1263-1280.

[70] G. Li, Z. Li, J. Chen, X. Chen, S. Qiao, S. Wang, Y. Xu, Y. Mai, Self-powered, high-speed Sb_2Se_3/Si heterojunction photodetector with close spaced sublimation processed Sb_2Se_3 layer, J. Alloys Compd. 737 (2018) 67-73.

[71] J. Cao, B. Xu, H. Lin, B. Luo, S. Chen, Novel heterostructured Bi_2S_3/BiOI photocatalyst: facile preparation, characterization and visible light photocatalytic performance, Dalton Trans. 41 (2012) 11482-11490.

[72] Y. Feng, C. Liu, H. Che, J. Chen, K. Huang, C. Huang, W. Shi, The highly improved visible light photocatalytic activity of BiOI through fabricating a novel p–n heterojunction BiOI/WO_3 nanocomposite, CrystEngComm 18 (2016) 1790-1799.

[73] A. Lagunin, A. Zakharov, D. Filimonov, V. Poroikov, QSAR Modelling of Rat Acute Toxicity on the Basis of PASS Prediction, Mol. Inf. 30 (2011) 241-250.

[74] X. Liu, J. Chen, M. Luo, M. Leng, Z. Xia, Y. Zhou, S. Qin, D. Xue, L. Lv, H. Huang, D. Niu, J. Tang, Thermal Evaporation and Characterization of Sb_2Se_3 Thin Film for Substrate Sb_2Se_3/CdS Solar Cells, ACS Appl. Mater. Interfaces 6 (2014) 10687-10695.

Figure captions

Fig. 1. XRD patterns taken from the pure Sb_2Se_3, SN-2.5%, SN-5%, SN-10% and SN-15% samples: (a) bulks and (b) powders.

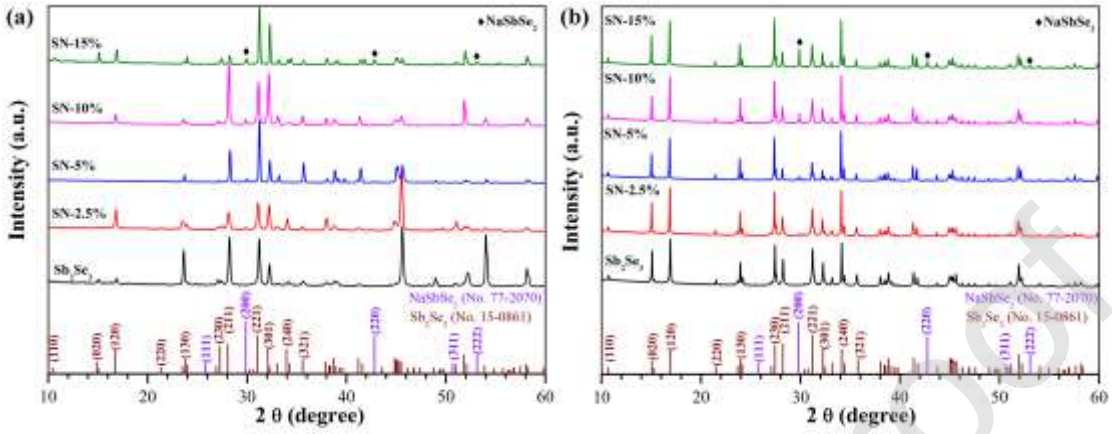

Fig. 2. The liquids projection of Na-Sb-Se system [27].

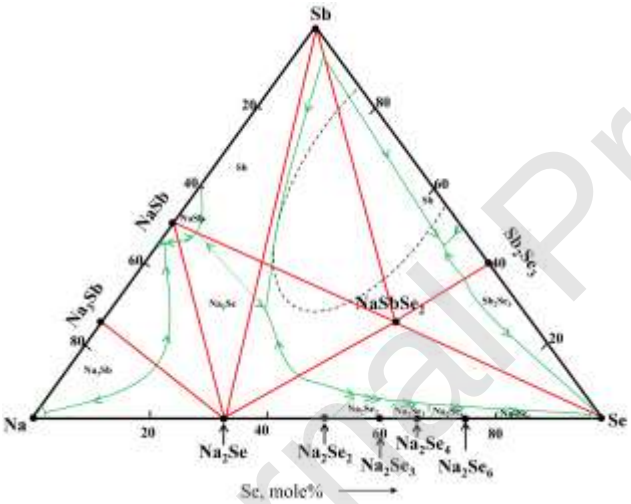

Fig. 3. Backscattered electron images of (a) SN-2.5% and (b) SN-15%. (c-e) the X-ray elemental mappings for Sb, Se, and Na in (b), respectively.

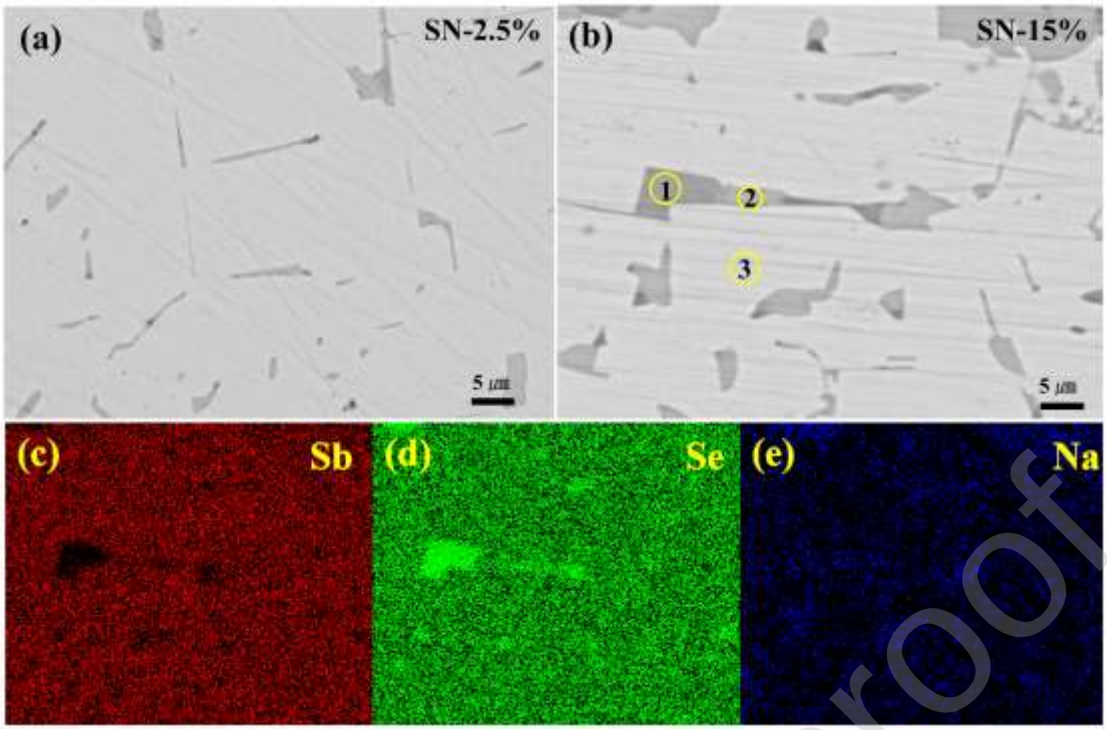

Fig. 4. Backscattered electron micrograph of etched surface of SN-15% sample and the X-ray elemental mappings for Sb, Se, and Na, respectively.

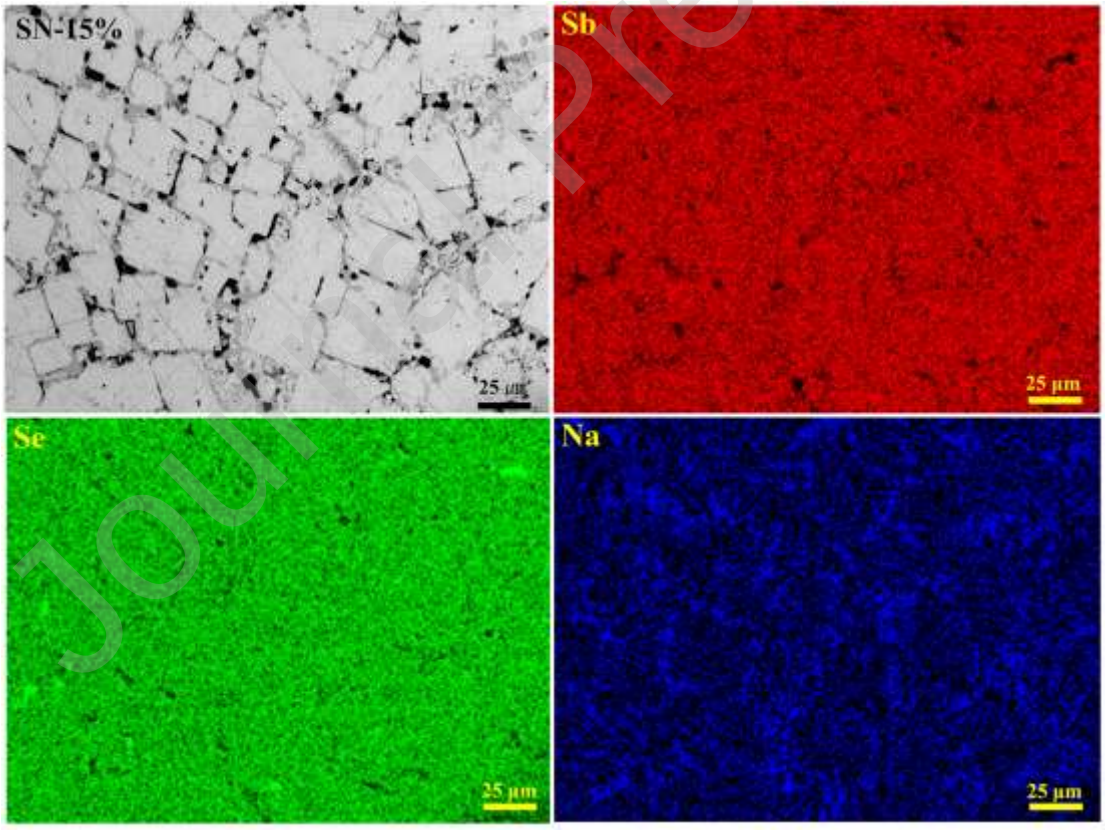

Fig. 5. The I-V curve of SN-2.5% sample in the voltage range of -0.8 to 0.8 V. Inset is

the schematic illustration of the sample during measurement process.

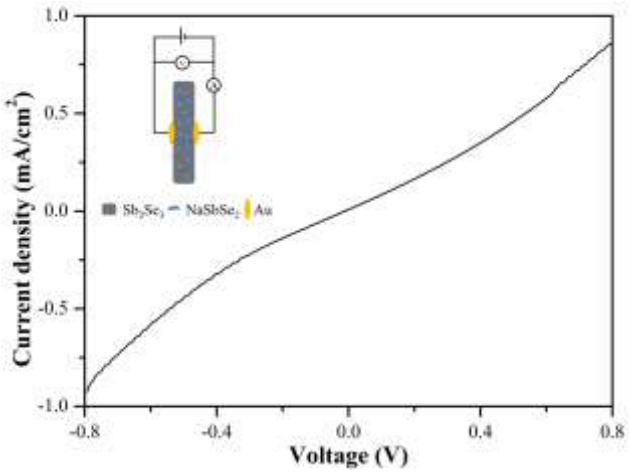

Fig. 6. Tauc plot of pure Sb_2Se_3, $NaSbSe_2$, SN-2.5%, SN-5%, SN-10% and SN-15% samples.

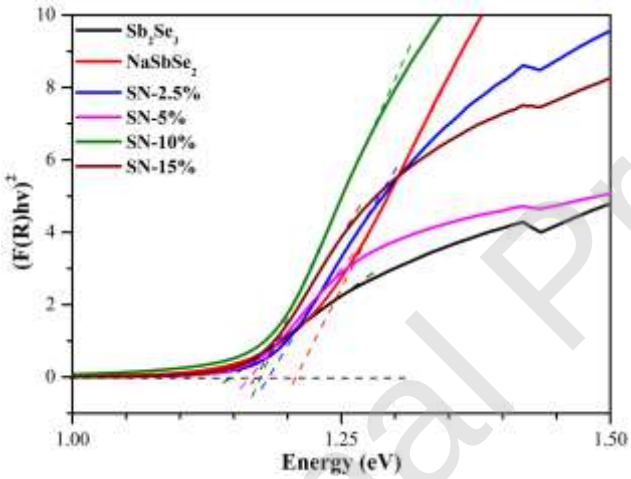

Fig. 7. The frequency dependence of impedance real (Z′) part, impedance imaginary (Z″) part, and normalized Z″ at different temperatures: (a-c) SN-2.5%; (d-f) SN-15%.

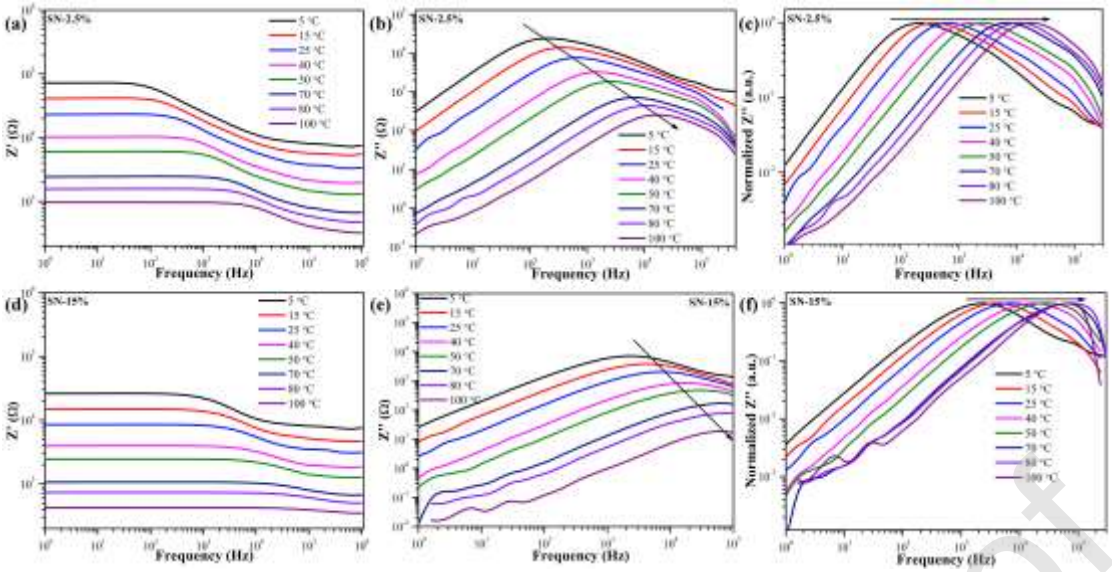

Fig. 8. Complex impedance plots of Z' versus Z″ (Nyquist plot) at different temperatures: (a) SN-2.5%; (b) SN-15%. (c) Complex impedance spectrum of composites with electrical equivalent circuit (inset) at 25 °C. (d) Conductivity of composites as a function of temperature.

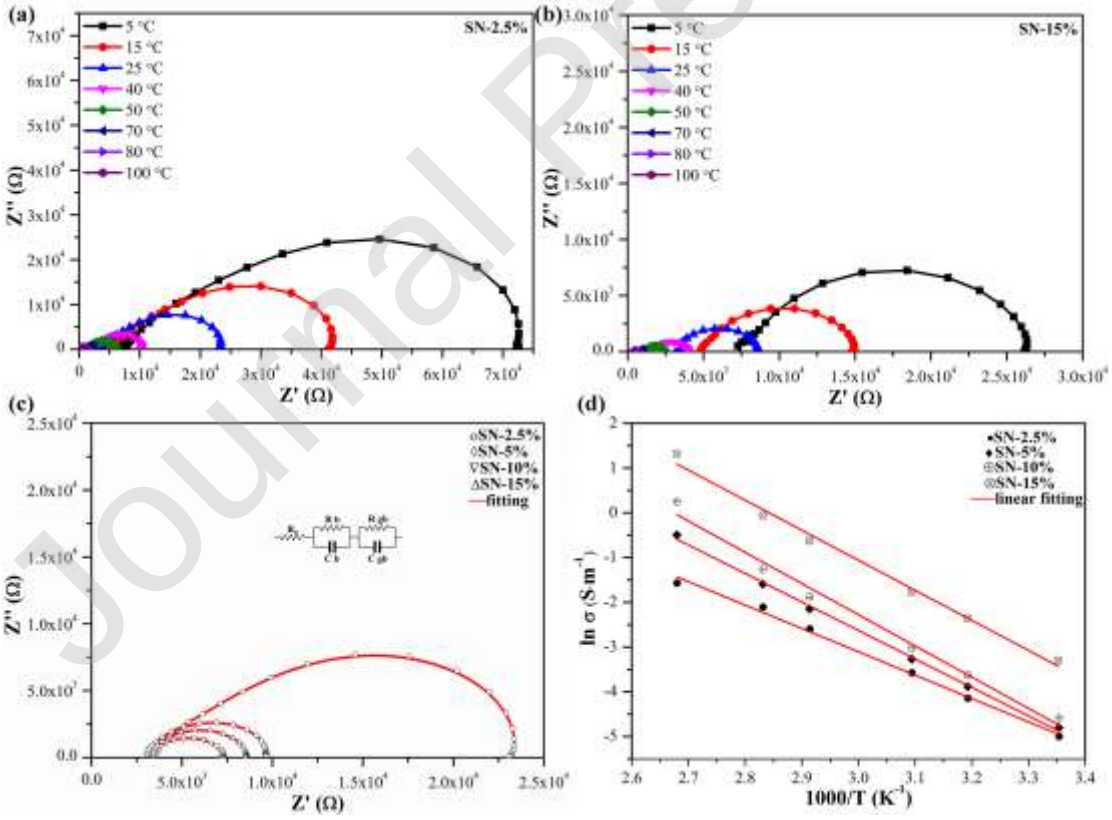

Fig. 9. Photoelectrochemical response of pure Sb_2Se_3, SN-2.5%, SN-5%, SN-10% and

SN-15% samples illuminated with a chopped light power density of 7 mW/cm^2. Inset is the schematic diagram of the three-electrode configuration.

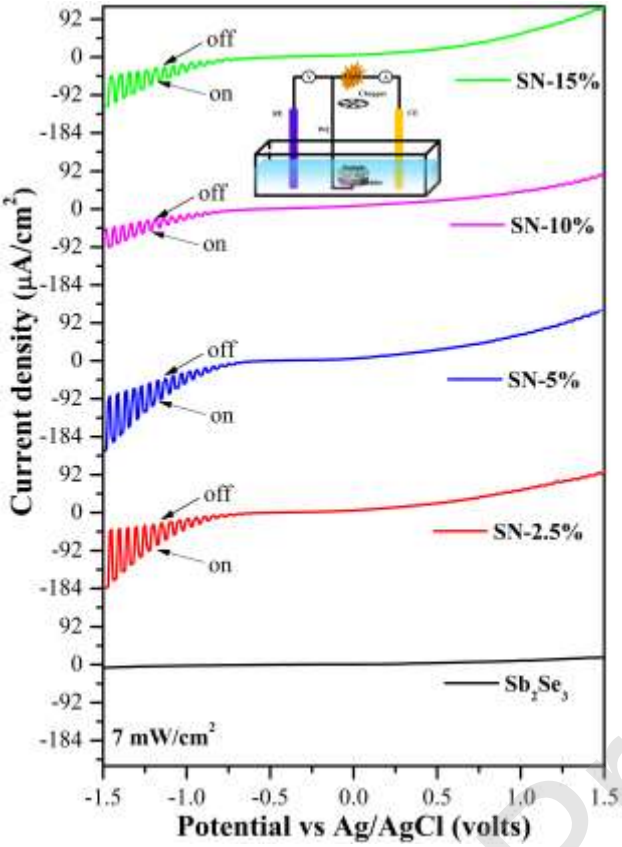

Fig. 10. (a) Time-resolved PEC photoresponse of pure Sb_2Se_3 and composites at light power density of 17.6 mW/cm^2 at -0.7 V. (b) The incident light intensity dependence of current density at a bias voltage of -0.7 V.

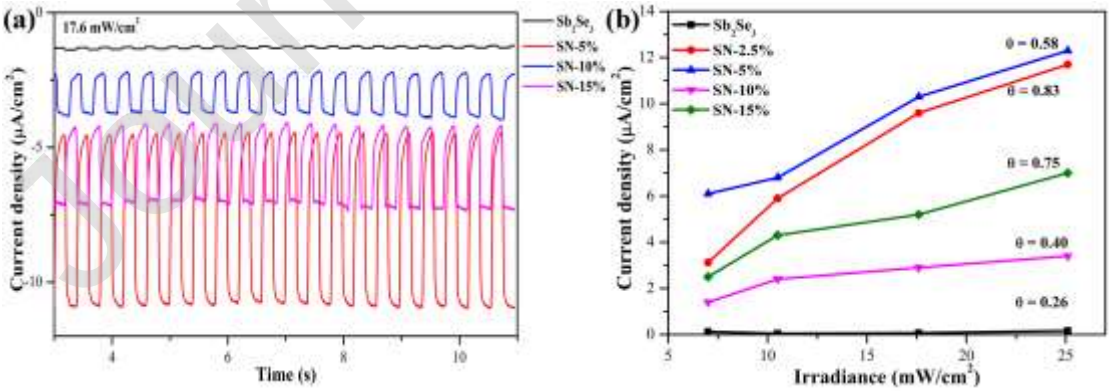

Fig. 11. Schematic illustration for the separation and transfer of photogenerated charges in the region of the interface between the Sb_2Se_3 and the $NaSbSe_2$.

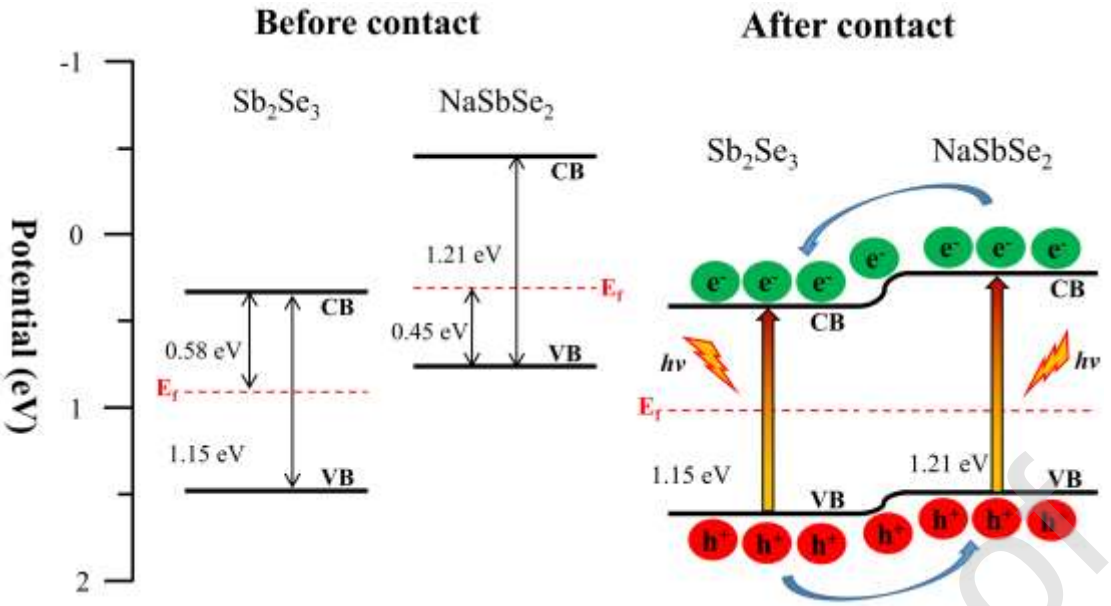

Table captions

Table 1. The compositions of points 1, 2 and 3 in SN-15% sample.

Point	Composition (at.%)		
	Na	Sb	Se
1	0	2.48	97.52
2	24.6	25.3	50.1
3	0.22	39.34	60.44

Table 2. After NaOH (1 M) etching, the compositions of white and gray areas in SN-15% sample.

Area	Composition (at.%)		
	Na	Sb	Se
white	0.55	39.34	60.11
gray	15.01	29.94	55.05

Table 3. The energy gap values of all compounds.

Sample	Sb_2Se_3	$NaSbSe_2$	SN-2.5%	SN-5%	SN-10%	SN-15%
Energy gap (eV)	1.15	1.21	1.18	1.16	1.17	1.17

Table 4. Values of R_{gb}, R_b, R_0, resistivity at 25 °C, and activation energy of Sb_2Se_3, $NaSbSe_2$, and composites.

Sample	R_{gb} (Ω)	R_b (Ω)	R_0 (Ω)	Resistivity (Ω·cm)	Activation energy (eV)
Sb_2Se_3	2.60×10^5	4.02×10^5	—	2.14×10^6	0.61
$NaSbSe_2$	1.44×10^6	8.63×10^3	—	8.87×10^5	0.45
SN-2.5%	1.55×10^4	4.07×10^3	3.70×10^3	1.48×10^4	0.45
SN-5%	4.66×10^3	1.85×10^3	3.14×10^3	1.20×10^4	0.55
SN-10%	2.36×10^3	1.55×10^3	3.35×10^3	9.71×10^3	0.60
SN-15%	3.09×10^3	2.08×10^3	3.39×10^3	2.67×10^3	0.58